Theoretical, numerical and experimental study of geometrical parameters that affect anisotropy measurements in polarization-resolved SHG microscopy.

Claire Teulon, Ivan Gusachenko, Gaël Latour, Marie-Claire Schanne-Klein

Theoretical, numerical and experimental study of geometrical parameters that affect anisotropy measurements in polarization-resolved SHG microscopy

Claire Teulon,[1] Ivan Gusachenko,[1,2] Gaël Latour[3] and Marie-Claire Schanne-Klein[1,*]

[1]*Laboratoire d'Optique et Biosciences, Ecole Polytechnique, CNRS, Inserm U1182, 91128 Palaiseau, France*

[2]*Okinawa Institute of Science and Technology, 1919-1 Tancha, Onna-son, Kunigami-gun Okinawa, Japan 904-0495*

[3]*Laboratoire Imagerie et Modélisation en Neurobiologie et Cancérologie, Université Paris-Sud, CNRS, 91405 Orsay, France*

marie-claire.schanne-klein@polytechnique.edu

Abstract: Polarization-resolved second harmonic generation (P-SHG) microscopy is an efficient imaging modality for *in situ* observation of biopolymers structure in tissues, providing information about their mean in-plane orientation and their molecular structure and 3D distribution. Nevertheless, P-SHG signal build-up in a strongly focused regime is not throroughly understood yet, preventing reliable and reproducible measurements. In this study, theoretical analysis, vectorial numerical simulations and experiments are performed to understand how geometrical parameters, such as excitation and collection numerical apertures and detection direction, affect P-SHG imaging in homogeneous collagen tissues. A good agreement is obtained in tendon and cornea, showing that detection geometry significantly affects the SHG anisotropy measurements, but not the measurements of collagen in-plane orientation.

OCIS codes: (180.4315) Nonlinear microscopy; (190.2620) Harmonic generation and mixing; (120.5410) Polarimetry; (170.3660) Light propagation in tissues; (170.6935) Tissue characterization.

References and links

1. P. Stoller, K. M. Reiser, P. M. Celliers, and A. M. Rubenchik, "Polarization-modulated second harmonic generation in collagen," Biophys. J. **82**, 3330–3342 (2002).
2. F. Tiaho, G. Recher, and D. Rouède, "Estimation of helical angles of myosin and collagen by second harmonic generation imaging microscopy," Opt. Express **15**, 12286–12295 (2007).
3. A. Erikson, J. Örtegren, T. Hompland, C. Davies de Lange, and M. Lindgren, "Quantification of the second-order nonlinear susceptibility of collagen I using a laser scanning microscope," J. Biomed. Optics **12**, 044002 (2007).
4. X. Han, R. M. Burke, M. L. Zettel, P. Tang, and E. B. Brown, "Second harmonic properties of tumor collagen: determining the structural relationship between reactive stroma and healthy stroma," Opt. Express **16**, 1846–1859 (2008).
5. S. Psilodimitrakopoulos, D. Artigas, G. Soria, I. Amat-Roldan, A. M. Planas, and P. Loza-Alvarez, "Quantitative discrimination between endogenous SHG sources in mammalian tissue, based on their polarization response," Opt. Express **17**, 10168–10176 (2009).

#234705 - $15.00 USD Received 17 Feb 2015; revised 23 Mar 2015; accepted 23 Mar 2015; published 2 Apr 2015

6. V. Nucciotti, C. Stringari, L. Sacconi, F. Vanzi, L. Fusi, M. Linari, G. Piazzesi, V. Lombardi, and F. S. Pavone, "Probing myosin structural conformation in vivo by second-harmonic generation microscopy," Proc. Natl. Acad. Sci. USA **107**, 7763–7768 (2010).
7. I. Gusachenko, G. Latour, and M.-C. Schanne-Klein, "Polarization-resolved second harmonic microscopy in anisotropic thick tissues," Opt. Express **18**, 19339–19352 (2010).
8. S. Psilodimitrakopoulos, V. Petegnief, N. d. Vera, O. Hernandez, D. Artigas, A. M. Planas, and P. Loza-Alvarez, "Quantitative imaging of microtubule alteration as an early marker of axonal degeneration after ischemia in neurons," Biophys. J. **104**, 968975 (2013).
9. C. P. Brown, M. A. Houle, K. Popov, M. Nicklaus, C. A. Couture, M. Laliberte, T. Brabec, A. Ruediger, A. J. Carr, A. J. Price, H. S. Gill, L. Ramunno, and F. Legare, "Imaging and modeling collagen architecture from the nano to micro scale," Biomed. Opt. Express **5**, 233–243 (2014).
10. P. Stoller, P. M. Celliers, K. M. Reiser, and A. M. Rubenchik, "Quantitative second-harmonic generation microscopy in collagen," Appl. Opt. **42**, 5209–5219 (2003).
11. S. V. Plotnikov, A. C. Millard, P. J. Campagnola, and W. A. Mohler, "Characterization of the myosin-based source for second-harmonic generation from muscle sarcomeres," Biophys. J. **90**, 693703 (2006).
12. A. E. Tuer, M. K. Akens, S. Krouglov, D. Sandkuijl, B. C. Wilson, C. M. Whyne, and V. Barzda, "Hierarchical model of fibrillar collagen organization for interpreting the second-order susceptibility tensors in biological tissue," Biophys. J. **103**, 2093–2105 (2012).
13. I. Gusachenko, V. Tran, Y. Goulam Houssen, J.-M. Allain, and M.-C. Schanne-Klein, "Polarization-resolved second-harmonic generation in tendon upon mechanical stretching," Biophys. J. **102**, 2220–2229 (2012).
14. J. Duboisset, A. Dora, and M. Roche, "Generic model of the molecular orientational distribution probed by polarization-resolved Second Harmonic Generation," Phys. Rev. A **85**, 1–25 (2012).
15. V. Ajeti, O. Nadiarnykh, S. M. Ponik, P. J. Keely, K. W. Eliceiri, and P. J. Campagnola, "Structural changes in mixed Col I/Col V collagen gels probed by SHG microscopy: implications for probing stromal alterations in human breast cancer," Biomed. Opt. Express **2**, 2307–2316 (2011).
16. D. Sandkuijl, A. E. Tuer, D. Tokarz, J. E. Sipe, and V. Barzda, "Numerical second- and third-harmonic generation microscopy," J. Opt. Soc. Am. B **30**, 382 (2013).
17. D. Rouède, J.-J. Bellanger, E. Schaub, G. Recher, and F. Tiaho, "Theoretical and experimental SHG angular intensity patterns from healthy and proteolysed muscles," Biophys. J. **104**, 1959–1968 (2013).
18. M. Rivard, C. A. Couture, A. K. Miri, M. Laliberte, A. Bertrand-Grenier, L. Mongeau, and F. Legare, "Imaging the bipolarity of myosin filaments with interferometric second harmonic generation microscopy," Biomed. Opt. Express **4**, 2078–2086 (2013).
19. R. M. Williams, W. R. Zipfel, and W. W. Webb, "Interpreting second-harmonic generation images of collagen I fibrils," Biophys. J. **88**, 1377–1386 (2005).
20. A. E. Tuer, S. Krouglov, N. Prent, R. Cisek, D. Sandkuijl, K. Yasufuku, B. C. Wilson, and V. Barzda, "Nonlinear optical properties of type I collagen fibers studied by polarization dependent second harmonic generation microscopy," J. Phys. Chem. B **115**, 12759–12769 (2011).
21. G. Latour, I. Gusachenko, L. Kowalczuk, I. Lamarre, and M.-C. Schanne-Klein, "In vivo structural imaging of the cornea by polarization-resolved second harmonic microscopy," Biomed. Opt. Express **3**, 1–15 (2012).
22. O. Nadiarnykh and P. J. Campagnola, "Retention of polarization signatures in SHG microscopy of scattering tissues through optical clearing," Opt. Express **17**, 5794–5806 (2009).
23. D. Aït-Belkacem, A. Gasecka, F. Munhoz, S. Brustlein, and S. Brasselet, "Influence of birefringence on polarization resolved nonlinear microscopy and collagen SHG structural imaging," Opt. Express **18**, 14859–14870 (2010).
24. I. Gusachenko and M.-C. Schanne-Klein, "Numerical simulation of polarization-resolved second-harmonic microscopy in birefringent media," Phys. Rev. A **88**, 053811 (2013).
25. L. Novotny and B. Hecht, *Principles of Nano-Optics* (Cambridge University, 2012), 2nd ed.
26. S. Hacyan and R. Jáuregui, "Evolution of optical phase and polarization vortices in birefringent media," J. Opt. A **11**, 085204 (2009).
27. P. C. Clemmow, "The theory of electromagnetic waves in a simple anisotropic medium," in "Proceedings of IEEE," , vol. 110 (1963), pp. 101–106.
28. R. LaComb, O. Nadiarnykh, S. Carey, and P. J. Campagnola, "Quantitative second harmonic generation imaging and modeling of the optical clearing mechanism in striated muscle and tendon," J. Biomed. Opt. **13**, 021109 (2010).
29. W. Zipfel, R. Williams, and W. Webb, "Nonlinear magic: multiphoton microscopy in the biosciences," Nature Biotechnol. **21**, 1369–1377 (2003).
30. D. M. Maurice, "The structure and transparency of the cornea," J. Physiol. **136**, 263–286 (1957).
31. D. A. D. Parry and A. S. Craig, "Quantitative electron microscope observations of the collagen fibrils in rat-tail tendon," **16**, 1015–1031 (1977).
32. D. W. Leonard and K. M. Meek, "Refractive indices of the collagen fibrils and extrafibrillar material of the corneal stroma," Biophys. J. **72**, 1382–1387 (1997).
33. A. N. Bashkatov, E. A. Genina, V. I. Kochubey, and V. V. Tuchin, "Estimation of wavelength dependence of

#234705 - $15.00 USD Received 17 Feb 2015; revised 23 Mar 2015; accepted 23 Mar 2015; published 2 Apr 2015

refractive index of collagen fibers of scleral tissue," Proc. SPIE **4162**, 265–268 (2000).
34. T. Starborg, N. S. Kalson, Y. Lu, A. Mironov, T. F. Cootes, D. F. Holmes, and K. E. Kadler, "Using transmission electron microscopy and 3View to determine collagen fibril size and three-dimensional organization," Nature Protocols **8**, 1433–1448 (2013).
35. P. Réfrégier, M. Roche, and S. Brasselet, "Precision analysis in polarization-resolved second harmonic generation microscopy," Opt. Lett. **36**, 2149–2151 (2011).

1. Introduction

Polarization-resolved second harmonic generation (P-SHG) microscopy has emerged as an essential modality in nonlinear optical microscopy to probe three-dimensional (3D) structures in biological tissues. This technique is of great interest to study biopolymers that exhibit strong endogenous SHG signals due to their dense non centrosymmetrical structures, such as myosin thick filaments, microtubules and collagen fibrils [1–9]. In particular, *in situ* visualization of fibrillar collagen in collagen-rich tissues, such as tendon, skin, bones or cornea, is crucial to understand how the 3D collagen network determines the tissue architecture and main properties. This is a major medical concern, whether to study collagen accumulation, impairment or disorder in numerous pathologies, or to characterize the structure of organs and guide tissular engineering.

Conventional SHG imaging relies on circularly polarized excitation light to efficiently image biopolymers without any preferred orientation within the focal plane. In contrast, P-SHG microscopy takes advantage of excitation with linear polarization at different angles to gain additional information about the optical anisotropy inherent to biopolymers in tissues [2–6, 9–14]. This modality therefore get insight into their structure from molecular scale to macroscopic scale, like other studies based on measurements of the forward/backward SHG intensity ratio [15], of the SHG radiation patterns [16, 17] or of interferometric-SHG [18].

P-SHG provides two types of information: the mean orientation φ of collagen fibrils in the field of view, and the SHG anisotropy parameter ρ, which reflects the relative SHG efficiency for excitation polarization parallel versus perpendicular to this main direction. This anisotropy parameter is directly related to the 3D collagen structure inside the SHG excitation volume, giving information about the molecular structure of collagen fibrils and their 3D distribution (disorder, main orientation) at the submicrometric scale.

However, accurate measurement of this anisotropy parameter ρ is not simple. Several experimental measurements of this parameter with forward detection have been reported for type I collagen in various tissues including tendon, lung and cornea [2, 7, 10, 19–21] and they ranged from 1.1 to 2.6. Moreover, P-SHG measurements can be performed with forward (F-SHG) or backward (B-SHG) signal detection, and different values of anisotropy parameter have been reported for simultaneous measurements of B-SHG and F-SHG [21]. This is a critical issue, since B-SHG is needed for *in vivo* P-SHG measurements. .

Many processes may indeed affect the tissue response, such as disrupted optical propagation within thick tissues due to birefringence, polarization scrambling or diattenuation [1, 7, 22, 23]. The focusing and detection numerical apertures (NA) have also been reported to affect anisotropy parameter measurements in thin collagen fibrils [16]. To address these issues, we recently reported vectorial numerical simulations of forward-detected P-SHG microscopy with a strongly focused beam [24]. Nevertheless, the combined role of detection directionality and focusing NA has never been addressed to the best of our knowledge.

The aim of this paper is to fully characterize how geometrical parameters may affect SHG anisotropy measurements, in order to guide the implementation of reliable and reproducible measurements. This study combines theoretical analysis, numerical calculations and experiments in homogeneous collagen-rich tissue. First, the theoretical formalism for P-SHG is introduced, which is necessary to understand how strong focusing can affect anisotropy. Numerical

#234705 - $15.00 USD Received 17 Feb 2015; revised 23 Mar 2015; accepted 23 Mar 2015; published 2 Apr 2015

simulations are then developed to account for imaging depth, focusing and collection NAs, and detection direction and calculate the SHG anisotropy parameter ρ as a function of those parameters. Finally, experiments are performed in rat-tail tendon and human cornea and compared with our numerical results.

2. Theoretical background

2.1. P-SHG microscopy basics in collagen tissues

The second harmonic (SH) response of a medium is characterized by its second order nonlinear susceptibility tensor $\chi^{(2)}$, which links the induced polarizability $\vec{P}^{2\omega}$ to the incident electric field $\vec{E}^{\omega}$:

$$P_i^{2\omega} = \chi_{ijk}^{(2)} E_j^{\omega} E_k^{\omega} \tag{1}$$

where i, j and k stand for x, y or z spatial directions. Assuming that fibrillar collagen exhibits a cylindrical symmetry and that Kleinmann symmetry applies, the tensor $\chi^{(2)}$ has only two independent components: $\chi_{xxx}^{(2)}$ and $\chi_{xyy}^{(2)} = \chi_{xzz}^{(2)} = \chi_{yxy}^{(2)} = \chi_{zxz}^{(2)} = \chi_{yyx}^{(2)} = \chi_{zzx}^{(2)}$, where x is the fibril axis.

In that case, the polarizability at 2ω writes [1]:

$$\begin{aligned} P_x^{2\omega} &= \chi_{xxx}^{(2)} E_x^2 + \chi_{xyy}^{(2)} E_y^2 + \chi_{xyy}^{(2)} E_z^2, \\ P_y^{2\omega} &= 2\chi_{xyy}^{(2)} E_x E_y \\ P_z^{2\omega} &= 2\chi_{xyy}^{(2)} E_x E_z \end{aligned} \tag{2}$$

As long as the fibrils and the incident electric field lie both within the focal plane, an incident electric field $\vec{E}_{inc}$ at angle α to the laboratory axis X induces the following SH polarization in the fibril frame (xyz):

$$\begin{aligned} P_x^{2\omega} &\propto \rho \cos^2(\alpha - \varphi) + \sin^2(\alpha - \varphi) \\ P_y^{2\omega} &\propto 2\cos(\alpha - \varphi)\sin(\alpha - \varphi) \end{aligned} \tag{3}$$

where $\rho = \frac{\chi_{xxx}^{(2)}}{\chi_{xyy}^{(2)}}$ is the anisotropy parameter and φ is the fibrils orientation angle, with respect to the axis X in the laboratory frame (see Fig. 1).

The total SHG signal intensity is then given by:

$$\mathscr{I}^{2\omega}(\alpha) = \beta[A\cos(4\alpha - 4\varphi) + B\cos(2\alpha - 2\varphi) + 1] \tag{4}$$

where A and B are related to susceptibility components and β gives the mean number of detected photons, which depends on the squared incident intensity and on geometrical parameters.

In P-SHG experiments, $\mathscr{I}^{2\omega}(\alpha)$ is measured for different laser excitation angles α. The orientation and ellipticity of the incident field is controlled by two waveplates inserted at the back of the objective (see Fig. 1). Two quantitative parameters are then obtained from $\mathscr{I}^{2\omega}(\alpha)$ either with a fit or a Fourier transform algorithm:

- the main direction of collagen fibrils, given by φ
- the anisotropy parameter, which reflects the anisotropy of the nonlinear response of these collagen fibrils. This ratio can be calculated as [7]:

$$\rho = \sqrt{\frac{A+B+1}{A-B+1}} = \sqrt{\frac{\mathscr{I}_{\parallel}}{\mathscr{I}_{\perp}}} \tag{5}$$

#234705 - $15.00 USD Received 17 Feb 2015; revised 23 Mar 2015; accepted 23 Mar 2015; published 2 Apr 2015

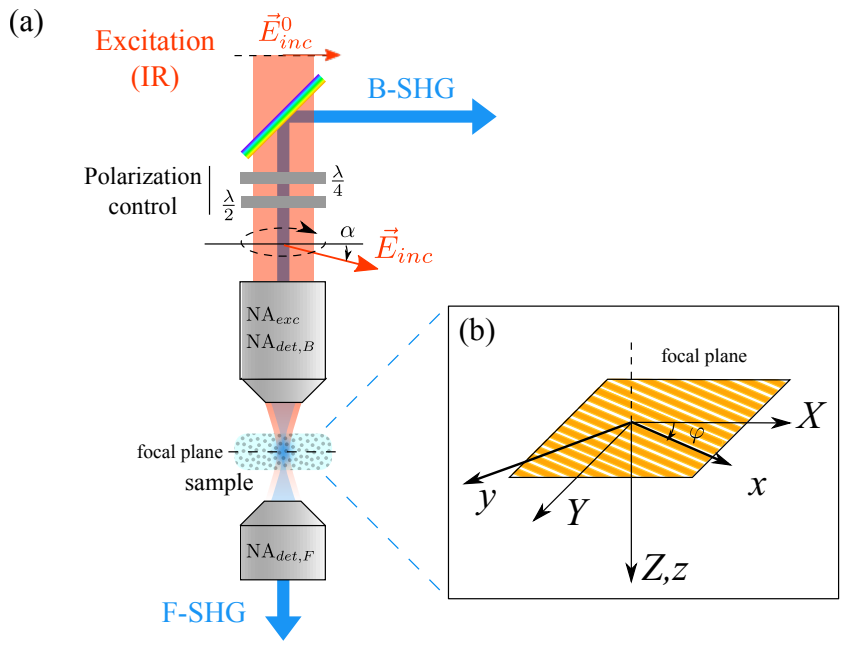

Fig. 1. (a) Setup geometry. Excitation polarization angle α is controlled by two achromatic waveplates. Excitation field $\vec{E}_{inc}$ is then focused through an objective (NA_{exc}). SH radiation is collected forwards with a condensor ($NA_{det,F}$) and backwards through the focusing objective ($NA_{det,B} = NA_{exc}$). (b) Zoom in the focal plane. (XYZ) is the laboratory frame, (xyz) is the fibril frame with x the fibril axis.

with $\mathscr{I}_{\parallel}$ and $\mathscr{I}_{\perp}$ the SH signal intensities for an incident electric field respectively parallel and perpendicular to the fibril orientation.

$$\begin{aligned} \mathscr{I}_{\parallel} &= \beta(A+B+1) \\ \mathscr{I}_{\perp} &= \beta(A-B+1) \end{aligned} \tag{6}$$

This approach is valid for both F-SHG and B-SHG signals. In order to simplify the problem, we will suppose from here on that collagen fibrils are oriented along X axis: $\varphi = 0$, so that xyz and XYZ frames are the same. $\vec{x}$, $\vec{y}$ and $\vec{z}$ are unitary vectors in x, y and z axis directions.

2.2. *Focal field in strongly focused regime*

Actually, the excitation electric field at focus is not within the focal plane because of the strong focusing needed to induce enough SH signal. The electric field follows the curvature of the incident wavefront, and an axial component of the incident field appears in the focal volume (see Fig. 2). Therefore, a vectorial description of the electric field is needed to account for polarization mixing due to strong focusing [24].

Figure 2 displays the simulated vectorial focal field $\vec{E}_{\parallel} = E_{x,\parallel}\vec{x} + E_{y,\parallel}\vec{y} + E_{z,\parallel}\vec{z}$ obtained from an incident electric field $\vec{E}_{inc}$ directed along x axis (i.e. parallel to fibrils direction) and focused with NA 1.2. The phase of $E_{x,\parallel}$, which is the main component, varies from $-\frac{\pi}{2}$ to $\frac{\pi}{2}$ over the axial extension of the excitation volume (Gouy phase shift). Yet it is set to 0 over the whole calculation volume in Fig. 2 to simplify the comparison with the y and z components. The intensity I_z of the axial component of the focal field represents approximately 12% of the

#234705 - $15.00 USD Received 17 Feb 2015; revised 23 Mar 2015; accepted 23 Mar 2015; published 2 Apr 2015

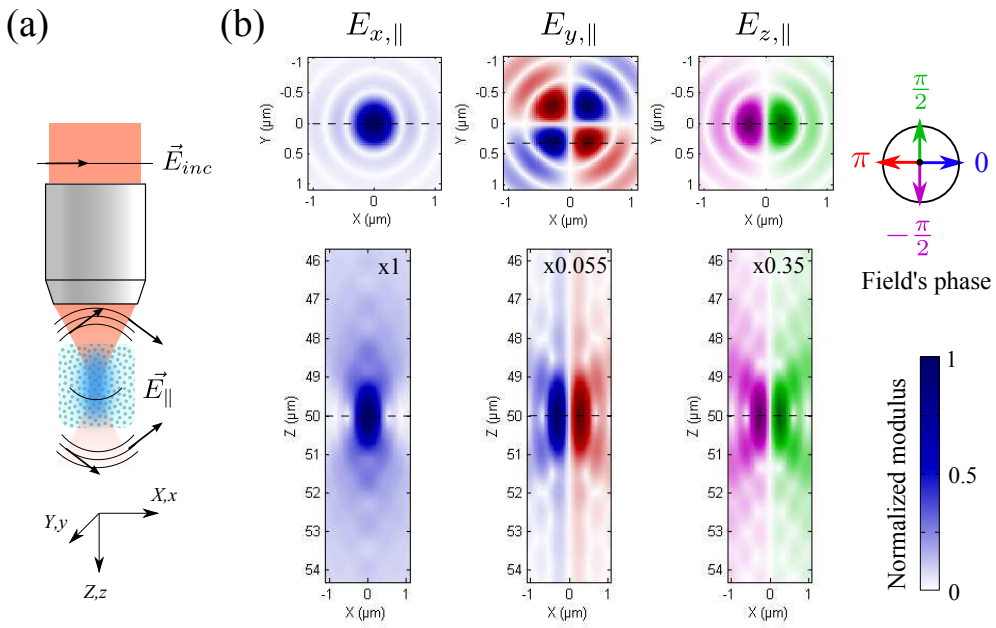

Fig. 2. Simulation of vectorial focal field $\vec{E}_{\parallel}$ for an incident electric field $\vec{E}_{inc}$ directed along x axis and NA=1.2 focusing. (a) Scheme of wavefront for strong focusing, showing the onset of an axial electric field component. (b) Modulus and phase of each electric field component $E_{x,\parallel}$, $E_{y,\parallel}$ and $E_{z,\parallel}$ in the laboratory frame. The modulus is represented by the color brightness, with the multiplication factor indicated in the upper right corner. The phase is color coded, with respect to $E_{x\parallel}$ phase set to 0 in the whole volume.

intensity I_x of the x component [16], which is not negligible. Furthermore, the phase of this axial component is shifted ($\pm\frac{\pi}{2}$) with respect to the one of $E_{x,\parallel}$. Regarding the y component of the focal field, $E_{y,\parallel}$, its intensity I_y is two orders of magnitude smaller than I_z. Its effects are therefore expected to be negligible.

2.3. *Nonlinear polarizability in strongly focused regime*

In this strongly focused regime, additional terms appear in the induced nonlinear polarizability $\vec{P}^{2\omega}$. We then obtain:

$$\begin{aligned}
P_x^{2\omega} &\propto (\rho E_{x,\parallel}^2 + E_{y,\parallel}^2 + E_{z,\parallel}^2)\cos^2\alpha \\
&\quad +(\rho E_{x,\perp}^2 + E_{y,\perp}^2 + E_{z,\perp}^2)\sin^2\alpha \\
&\quad +2(\rho E_{x,\parallel}E_{x,\perp} + E_{y,\parallel}E_{y,\perp} + E_{z,\perp}E_{z,\parallel})\cos\alpha\sin\alpha \\
P_y^{2\omega} &\propto 2E_{x,\parallel}E_{y,\parallel}\cos^2\alpha + 2E_{x,\perp}E_{y,\perp}\sin^2\alpha \\
&\quad +2(E_{x,\parallel}E_{y,\perp} + E_{y,\parallel}E_{x,\perp})\cos\alpha\sin\alpha \\
P_z^{2\omega} &\propto 2E_{x,\parallel}E_{z,\parallel}\cos^2\alpha + 2E_{x,\perp}E_{z,\perp}\sin^2\alpha \\
&\quad +2(E_{x,\parallel}E_{z,\perp} + E_{z,\parallel}E_{x,\perp})\cos\alpha\sin\alpha
\end{aligned} \tag{7}$$

where $\vec{E}_{\parallel}$ (resp. $\vec{E}_{\perp}$) are the focal fields for an incident electric field parallel (resp. perpendicular) to the fibrils direction, and α stands for the excitation polarization angle.

#234705 - $15.00 USD Received 17 Feb 2015; revised 23 Mar 2015; accepted 23 Mar 2015; published 2 Apr 2015

The anisotropy parameter ρ is nevertheless still determined with Eq. (3) and (4), i.e. considering that the fibrils and the incident electric field both lie within the focal plane. Artifacts due to the additional terms in the nonlinear polarizability therefore appear when the focal field exhibit axial components due to strong focusing, or alternatively when the fibril's distribution cannot be described in 2D.

The terms $E_{x,\parallel}^2$, $E_{x,\parallel}E_{y,\perp}$ and $E_{y,\perp}^2$, with $E_{x,\parallel} = E_{y,\perp}$, are the only ones present when the incident electric field lies within the focal plane. In that 2D case, Eq. (7) simplifies to Eq. (3) and the anisotropy parameter ρ is measured precisely.

In a strongly focused regime, the strongest terms besides $E_{x,\parallel}^2$, $E_{x,\parallel}E_{y,\perp}$ and $E_{y,\perp}^2$ in the nonlinear polarizability $\vec{P}^{2\omega}$ are $E_{x,\parallel}E_{z,\parallel}$, $E_{x,\parallel}E_{z,\perp}$, $E_{z,\parallel}^2$ and $E_{z,\perp}^2$. The term $E_{z,\parallel}E_{z,\perp}$ is actually very small because there is almost no overlap between $E_{z,\perp}$ and $E_{z,\parallel}$ amplitudes in the focal volume (see I_z in Fig. 2(b)). Consequently, we expect that:

- $P_x^{2\omega}$ is modified by the axial components $E_{z,\parallel}$ or $E_{z,\perp}$ of the focal field. The induced SH radiation is therefore also modified: its intensity changes, as well as its spatial pattern because of symmetry breaking.
- $P_y^{2\omega}$ changes are negligible
- An axial component $P_z^{2\omega}$ appears: its emission in the backward and forward directions can be observed because of the high detection NA. This axial component exhibits a specific radiation pattern and induces changes in the SH radiated field.

Numerical simulations are required to calculate those modified radiation patterns due to strong focusing and to understand how much they affect the measurement of anisotropy parameter ρ.

3. Numerical simulations

3.1. Scheme of theoretical approach

All numerical simulations were performed with a vectorial description of the electric fields to account for polarization mixing due to strong focusing. As in Fig. 2, the electric field distribution was calculated all around the focal volume to account for phase variations within this region. The main steps of this calculation were the following, as precisely described in [24]:

1. The starting point of the calculation was the incident field orientation at the backpupil of the objective. The objective transforms this incident plane field in a spherical wave converging in the focal plane.
2. For a fixed position of the objective, i.e. a fixed depth in the sample, propagation of this spherical wave was simulated in the immersion medium and then in the sample. From objective to interface, propagation was described by angular spectrum representation method [25]. Boundary conditions were used to obtain the field in the sample near the surface. The focal field distribution was then calculated by a method similar to angular spectrum representation, but with different field propagators for ordinary and extraordinary waves [26], in order to account for propagation in anisotropic media such as tendon.
3. The obtained focal field distribution was used to calculate the induced nonlinear polarizability of the medium using Eq. (7).

#234705 - $15.00 USD Received 17 Feb 2015; revised 23 Mar 2015; accepted 23 Mar 2015; published 2 Apr 2015

4. Finally, radiation of the SHG signal was calculated using Clemmow scaling method [27]. We obtained an intensity pattern $I_\Omega(\alpha)$ for a given orientation α of the laser excitation field, where $\Omega = (\theta, \psi)$ represents the radiation direction. We then calculated the total SHG signal intensity $\mathscr{I}(\alpha)$ by integrating $I_\Omega(\alpha)$ over the full solid angle of detection.

This procedure was performed for different polarization angles α of the laser excitation field with respect to the X axis. The anisotropy parameter ρ was then extracted from the obtained total SHG signal intensity $\mathscr{I}(\alpha)$ using Eq. (4) and (5).

We used this method to calculate ρ for forward (F-SHG) and backward (B-SHG) detection, for different focusing NAs and different collection NAs of the radiated field, at increasing depth within the sample.

All these calculations were performed in homogeneous media with aligned collagen fibrils within the whole excitation volume, such as the model tissue described next, tendon or cornea. The optical parameters that needed to be taken into account were the immersion medium, the refractive index of this medium, the sample birefringence and dispersion, and of course the intrinsic value of the anisotropy parameter ρ without any focusing effect.

We first studied a basic model system to understand how strong focusing affects the measurement of anisotropy parameter ρ, both in F-SHG and B-SHG. We considered a homogeneous model system with aligned collagen fibrils oriented along X axis, with the same refractive index as the immersion medium (water, $n = 1.33$), no dispersion and no birefringence. There were no effects on the incident electric field except basic propagation. The intrinsic value of collagen anisotropy parameter ρ without any focusing effect was fixed to 1.36, which was obtained from our experimental data in stretched rat-tail tendon with moderate focusing (NA 0.95) and forward detection [13].

3.2. SH radiation diagrams and anisotropy

Figure 3 shows the spatial distribution in the focal volume (modulus and phase) of $E^2_{x,\parallel}$ and of the additional terms in the nonlinear polarizability and their radiation patterns in the far field, for both forward and backward detections. The directions in the far field are labeled with n_x and n_y, defined as $n_x = n\sin\theta\cos\psi$ and $n_y = n\sin\theta\sin\psi$ with n the refractive index in the sample, and θ and ψ the angles describing the radiation direction [24]. The radiation pattern then corresponds to a 2D projection in the (xy) plane of the wavefront intensity.

Those terms affect anisotropy measurements as follows:

1. $E_{x,\parallel}E_{z,\parallel}$ and $E_{x,\parallel}E_{z,\perp}$ terms have an antisymmetric amplitude distribution in the focal volume (Fig. 3(b_1) and 3(b_2)): their intensity has a symmetric distribution but their phase shifts from $\frac{\pi}{2}$ to $-\frac{\pi}{2}$ through the symmetry plane. It results in a similar symmetry in the far field radiation pattern and a π phase shift between backward and forward radiation (Fig. 3(d_1) and 3(d_2)).

2. $E^2_{z,\parallel}$ and $E^2_{z,\perp}$ terms have a symmetric amplitude distribution in the focal volume (Fig. 3(a_2) and 3(a_3)). It results in a similar symmetry in the far field radiation pattern, but no phase shift between backward and forward radiations, which are both in phase with $E^2_{x,\parallel}$ radiation (Fig. 3(c_2) and 3(c_3)).

All of those additional terms have a broad radiation pattern, with no intensity at small collection NAs. They induce a change in anisotropy measurement at high collection NA only.

The effect of these additional terms on SHG anisotropy parameter ρ can be estimated by looking at the spatial pattern of the intensity ratio $\sqrt{\frac{I_\parallel}{I_\perp}}$ depicted in Fig. 4(a), reminding that $\rho = \sqrt{\frac{\mathscr{I}_\parallel}{\mathscr{I}_\perp}}$ after solid angle integration. $E_{x,\parallel}E_{z,\parallel}$ and $E^2_{z,\parallel}$ terms appear for an excitation parallel

#234705 - $15.00 USD Received 17 Feb 2015; revised 23 Mar 2015; accepted 23 Mar 2015; published 2 Apr 2015

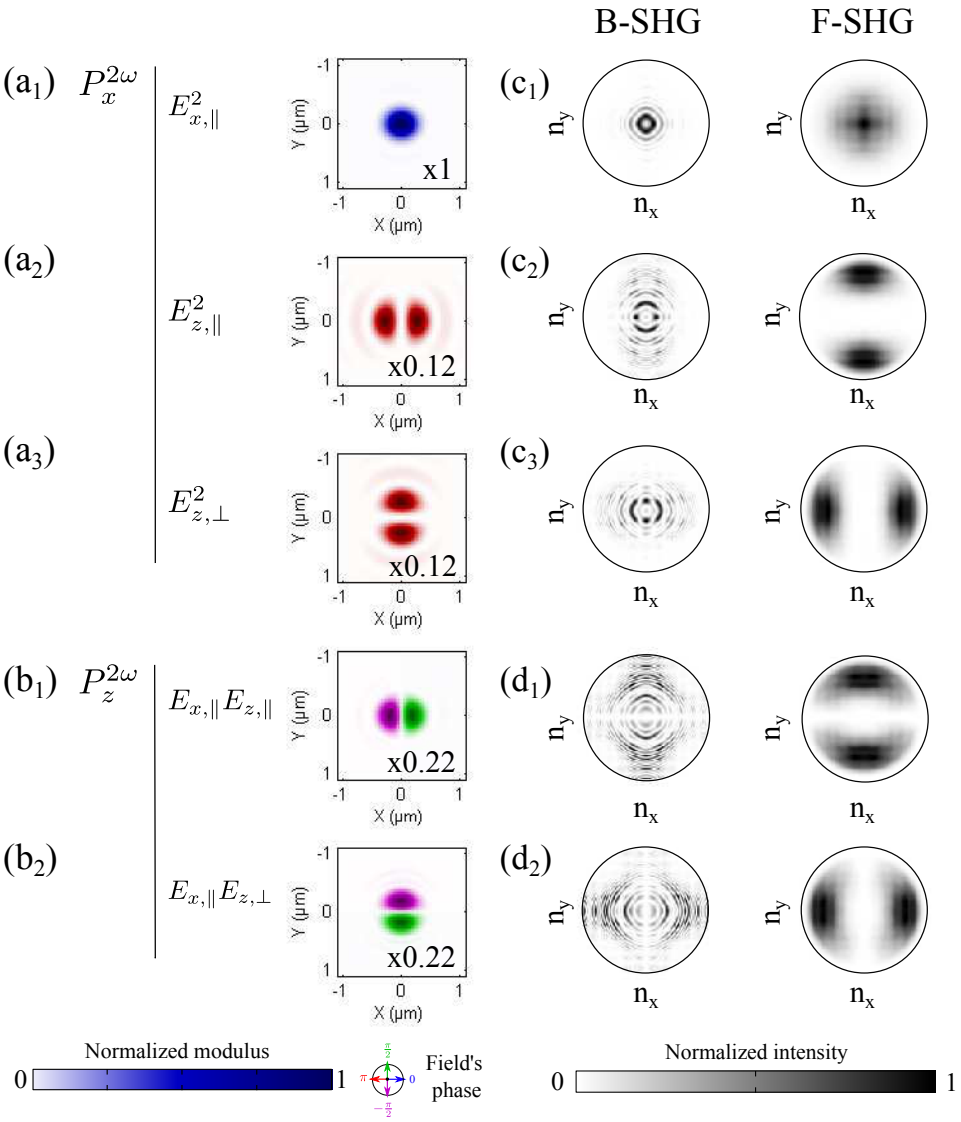

Fig. 3. (a-b) Spatial pattern of additional terms in the nonlinear polarizability due to strong focusing (excitation NA 1.2) compared to usual term $E^2_{x,\parallel}$ (a$_1$): (a) $\vec{P}^{2\omega}_x$, (b) $\vec{P}^{2\omega}_z$. The modulus is represented by the color brightness, with the multiplication factor indicated in the bottom. The phase is color coded with the same colors as in Fig. 2. (c-d) Backwards and Forward intensity radiation patterns induced by those additional terms, for the same excitation NA and collection NA 1.2 (black circle).

to x axis ($\alpha = 0$), i.e. contribute to $I_\parallel$, while $E^2_{z,\perp}$ appears for an excitation perpendicular to x axis ($\alpha = \frac{\pi}{2}$), i.e. contributes to $I_\perp$.

$E_{x,\parallel}E_{z,\parallel}$ contributes to the axial component of the nonlinear polarizability: it is negative in backward detection and has a positive value forwards. This term therefore increases $I_\parallel$ with respect to $I_\perp$, i.e. increases ρ in the forward direction. In the backward direction, the same term $E_{x,\parallel}E_{z,\parallel}$ decreases $I_\parallel$ with respect to $I_\perp$ because of its π phase shift with respect to other terms

#234705 - $15.00 USD Received 17 Feb 2015; revised 23 Mar 2015; accepted 23 Mar 2015; published 2 Apr 2015

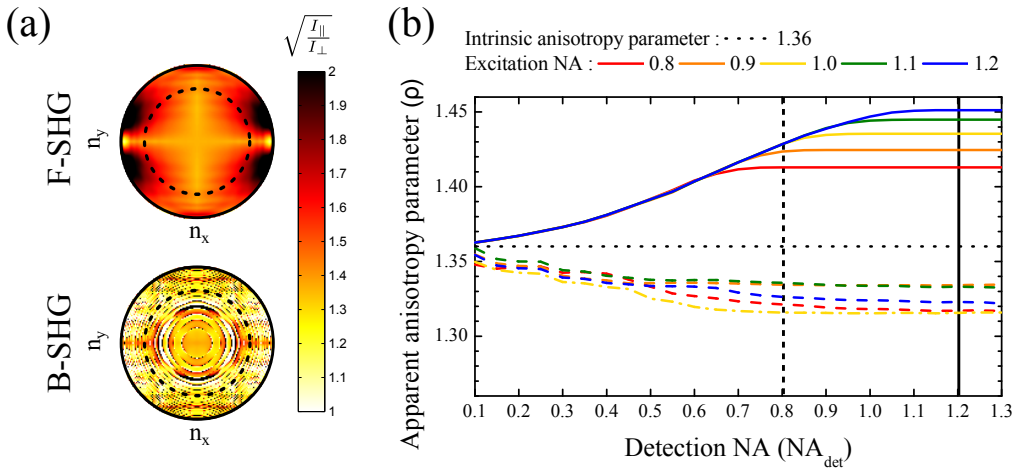

Fig. 4. (a) Spatial pattern of local intensities ratio $\sqrt{I_{\parallel}/I_{\perp}}$ backwards (bottom) and forwards (top). Full circle: collection NA=1.2, dashed circle: collection NA=0.8. (b) Anisotropy parameter ρ in respect to excitation and collection NA for B-SHG (dashed line) and F-SHG (full line) signals. Intrinsic value: $\rho = 1.36$. ρ is overestimated in forward measurements, underestimated in backward measurements. ρ values at collection NAs 0.8 and 1.2 are indicated by the vertical lines.

in the far field radiation. ρ is then underestimated. The effect of $E^2_{z,\parallel}$ and $E^2_{z,\perp}$ on $\sqrt{\frac{I_{\parallel}}{I_{\perp}}}$ ratio is harder to account for, but smaller. The term $E_{x,\parallel}E_{z,\perp}$ has no direct effect on ρ.

This is indeed what is observed in Fig. 4(b): the anisotropy parameter ρ is overestimated for forward detection, and underestimated for backward detection. The overestimation of ρ gets stronger when the collection NA is wider, since the detected SHG signal is integrated in a larger collection angle. For collection NA greater than the focusing NA, the determined value of ρ does not change anymore.

4. Experiments

4.1. Tendon and cornea preparation

Tendon Tendons were extracted from Sprague-Dawley rat-tails (female, ≈300g) kept frozen until dissection, and stored after dissection at 4°C in a solution containing 50% glycerol and 50% phosphate buffer saline (PBS). They were maintained overnight in this solution to perform optical clearing and avoid strong backscattering and scrambling of forward and backward detection channels when imaging the sample [28]. SHG imaging was performed within a few days, in combination with two-photon excited fluorescence imaging. Tendons were labeled with fluorescent latex beads (1 μm diameter, L1030, Sigma-Aldrich) to enable imaging of the very same area in the sample when changing the objective lens. After rinsing, they were stretched to get rid of the crimps and facilitate alignment of the fibrillar pattern. They were set in the PBS/glycerol mixture in a custom-built holder that maintained them between two coverslips in the focal plane of the microscope.

Cornea Human corneas that were unsuitable for transplantation due to low endothelial cell density were obtained from the French Eye Bank (BFY, Paris, France). They were fixed in a 4% paraformaldehyde (PFA) solution and stored at 4°C in a 1% PFA solution until SHG imaging.

#234705 - $15.00 USD Received 17 Feb 2015; revised 23 Mar 2015; accepted 23 Mar 2015; published 2 Apr 2015

Corneas were labeled with the same fluorescent latex beads as tendons (1 μm diameter, L1030, Sigma-Aldrich). Optical clearing was not necessary since corneas are naturally transparent. The same custom-built holder was used for SHG imaging, setting the cornea in a 1% PFA solution between two coverslips. In cornea, collagen is organized in a plywood-like structure composed of stacked lamellae containing thin fibrils aligned along a crystalline array. Two sequential lamellae show about perpendicular fibril directions. SHG imaging was performed on the posterior side of the cornea (near the endothelium) to observe the thickest lamellae (2 μm to 5 μm thickness). In that case, lamellae were thick enough to contain the whole excitation volume and the tissue could be considered as homogeneous when the excitation beam was focused inside a lamella.

4.2. Imaging setup

P-SHG imaging was performed using a custom-built laser scanning microscope as depicted in Fig. 1. Excitation was provided by a femtosecond Titanium-sapphire laser (Mai Tai, Spectra-Physics) tuned at 860 nm and scanned in the *xy* directions using galvanometric mirrors. It was focused in the sample using the following water-immersion objectives: 20x, 0.95NA (XLumPlanFl, Olympus); 40x, 1.1NA (LD C-Apochromat, Zeiss) or 60x, 1.2NA (UPlanApo, Olympus). The size of the excitation volume was measured to be 410 nm (resp. 360 nm, 340 nm) in the transverse direction and 1600 nm (resp. 1200 nm, 1600 nm) in the axial direction for the 20x (resp. 40x, 60x) objective, which is in good agreement with theoretical values [29]. Excitation power at the objective focus was adjusted using a rotating half waveplate and a Glan prism that filtered out y-polarization before entering the microscope setup. It was typically 5 mW (cornea) to 10 mW (tendon).

Forward SHG signal (F-SHG) was collected using an aplanatic condenser (U-AAC, Olympus) with effective NA $\approx$ 1.3, while backward SHG signal (B-SHG) was collected through the focusing objective and separated from the excitation path by a dichroic mirror (695DCXRU, Chroma). Both SHG signals were then detected using photon-counting photomultiplier tubes (P25PC, Electron Tubes) and appropriate spectral filters to reject the laser excitation (FF01-680SP, FF01-720SP, Semrock) and select SHG signal (FF01-427/10 interferential filter, Semrock). Neutral densities were sometimes used in the forward channel to balance intensities of F-SHG and B-SHG signals and avoid saturation of the detectors.

The polarization was controlled with two motorized achromatic waveplates (MRAC2/40070707M, Fichou, France) inserted at the backpupil of the objective [7]. A quarter waveplate was first used to correct the 14% ellipticity, mainly introduced by the galvanometric mirrors and the dichroic mirror, and obtain a well-defined linear polarization (ellipticity less than 4% for small scanning angles after correction). A half waveplate was then used to rotate this linear polarization and control its orientation.

All polarization-resolved images were acquired at 36 excitation angles α regularly spaced between 0°and 360°. Multimodal images were recorded in the same *xy* square area in the sample (72 μm x 72 μm, $\sim$200x200 pixels), using 100 kHz pixel rate, $\sim$0.4 μm pixel size and 1 or 5 μm *z*-step with each of the three different objectives. The depth z within the medium was related to the lens displacement dz_{lens} by $z = dz_{\text{lens}}\, n_{\text{medium}}/n_{\text{water}}$ because of the index mismatch between the medium and water.

4.3. Image analysis

The imaged area was divided in 100 square sub-areas (7.2 μm x 7.2 μm, $\sim$20x20 pixels). Both parameters φ and ρ were then extracted for each one of those sub-areas, at each recorded depth, using a fitting algorithm (the same results can be obtained with a Fourier transform algorithm as described in [8]). We kept only values with enough signal intensity, without any saturation

#234705 - $15.00 USD Received 17 Feb 2015; revised 23 Mar 2015; accepted 23 Mar 2015; published 2 Apr 2015

and with a good enough fitting quality, given by a r-squared parameter (r^2).

In tendon, we computed the mean value of ρ at each depth, only over the values determined with $r^2 > 0.95$.

In cornea, we used the r^2 values to discriminate the ρ values measured inside a lamella (homogeneous medium with well aligned fibrils) from those measured in between two lamellae. We indeed showed in [21] that in between two lamellae, where the excitation volume contains fibrils with two perpendicular directions, the anisotropy parameter ρ is underestimated, with a smaller r^2 value. We kept the ρ values determined with $r^2 > 0.99$ (F-SHG) or $r^2 > 0.95$ (B-SHG) and computed the mean value of those measurements over the whole depth of imaging.

We analyzed the expected measurement accuracy in our setup in order to estimate whether the variations of ρ as a function of various parameters were significant or not (see Appendix). The main noise in our setup was shot noise of detected photons. Considering that we detected around 200,000-300,000 photons (total number for all excitation angles) in each sub-area for the measurements reported in this paper, the measurement errors on orientation φ and anisotropy parameter ρ were $\Delta\varphi < 1^\circ$ and $\Delta\rho < 0.01$.

We also studied possible experimental artifacts due to different detection efficiency for different polarizations, mainly induced by the dichroic mirror. To that end, measurements were done in the same area of a tendon for two different sample orientations: one measurement with collagen fibrils oriented along x axis, the other one with collagen fibrils oriented along y axis. The measured error on ρ was only $\Delta\rho_{\mathrm{exp}} < 0.02$. It means that the slightly different reflectivity of the dichroic mirror for different polarizations detected in the backward channel is negligible for usual scanning angles.

5. Results and discussion

P-SHG experiments were performed in two tissues to verify numerical simulations with realistic parameters: tendon, where collagen fibrils are aligned along the same direction, and cornea, where collagen fibrils are organized in lamellae in a plywood-like structure, so that fibrils can be considered as aligned together in a lamella. These biological samples are therefore homogeneous 2D media as hypothesized in our numerical simulations.

Parameters used to perform numerical simulations in tendon and cornea were deduced from the literature and from Gladstone's and Dale's mixture law [30–34]. Birefringence is defined as $\Delta n = n_e - n_o$ with n_o the ordinary refractive index, and n_e the extraordinary one. Dispersion is defined as $d = (n^{2\omega} - n^{\omega})/n^{2\omega}$, in %, with $n^{2\omega}$ and n^{ω} the ordinary refractive indexes of the media respectively at 430 nm (SH wave) and 860 nm (incident wave). The refractive index n is given at 860 nm for an ordinary wave. For tendon, the chosen optical parameters were $n = 1.45$, $\Delta n = 0.007$ and $d = 3\%$. For cornea, $n = 1.37$, $\Delta n = 0$ and $d = 1.5\%$.

The intrinsic value of the anisotropy parameter ρ without any focusing effect was supposed to be 1.36 in cornea [7]. In tendon, optical clearing induced a significant swelling of the sample [28], and we considered that this swelling induced disorder. Simulations were therefore performed with an intrinsic ρ value of 1.5, slightly larger than our measurement in tendon, to take into account ρ increase due to disorder [13].

Experimental and simulated results are displayed in Fig. 5. In tendon, the simulated anisotropy parameter value at each depth is shown in Fig. 5(a) and compared with the mean measured value, which is displayed in 5(b). The goodness of fit r^2 for the experimental values is ≈ 0.98, except for the first data point, near the surface of the sample. We observe that the measured anisotropy is overestimated for forward measurements and underestimated backwards. According to the numerical simulations, the excitation NA seems to have no effect here. Simulated and experimental values show a good quantitative agreement, except for the experimental curve with the 20x objective (NA 0.95) which has a slight offset. This is probably due to the

#234705 - $15.00 USD Received 17 Feb 2015; revised 23 Mar 2015; accepted 23 Mar 2015; published 2 Apr 2015

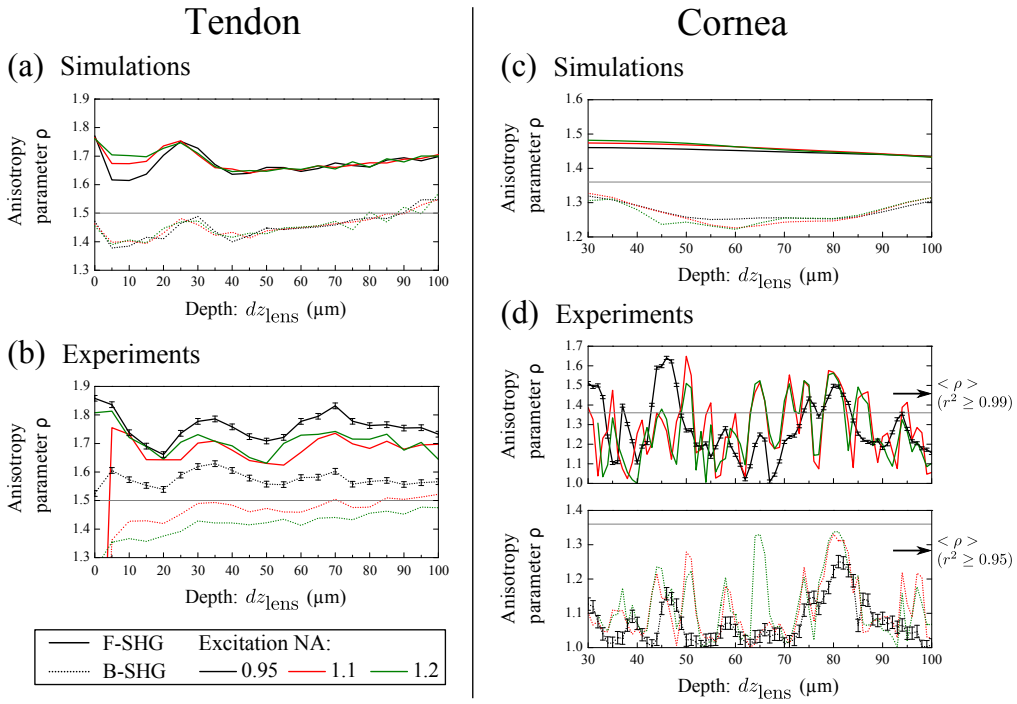

Fig. 5. Comparison between experimental results and numerical simulations. ρ intrinsic value is given by the full line in gray. **In tendon**: (a) numerical simulation, (b) mean experimental values of anisotropy parameter ρ at different depths for each of the three objectives and for F-SHG and B-SHG signals. **In cornea**: (c) numerical simulation, (d) mean experimental values of ρ at different depths for each of the three objectives and for F-SHG and B-SHG signals. $dz_{\text{lens}} = 0\ \mu m$ at the surface of the sample.

larger excitation volume probed using this objective, which results in a measurement more sensitive to disorder, so that ρ is overestimated.

In cornea, the numerical and experimental ρ values are displayed in Fig. 5(c) and 5(d). We observe the same qualitative results as for tendon: ρ is overestimated forwards, underestimated backwards, and excitation NA has almost no effect. Experimental curves nevertheless differ from the simulated ones because the cornea is not a homogeneous medium in contrast to the medium used for simulation, but has a plywood-like structure. As observed in Fig. 5(d), in between two lamellae, where the excitation volume contains fibrils with two perpendicular directions, ρ is underestimated and is determined with a lower r^2 factor as explained in section 4.3 (see also Fig. 7 of [21]). The experimental curve with the 20x objective (NA 0.95) is smoother, probably due to the larger excitation volume. It is therefore more relevant to compare the mean value of ρ only inside lamellae over the whole depth of imaging, that is for $r^2 > 0.99$ (F-SHG) or 0.95 (B-SHG). In that case, we obtain a good quantitative agreement between experiments and simulations (see Table 1).

All our experimental measurements are thus in good agreement with our numerical simulations considering additional terms in the nonlinear polarizability due to strong focusing. It confirms our theoretical expectation that strong focusing mainly affects the determination of the anisotropy parameter ρ. It shows opposite effects for forward and backward directions due to the opposite phase of SH radiation by these additional terms in forward and backward directions. Practically, ρ is overestimated for forward detection and underestimated with backward

#234705 - $15.00 USD Received 17 Feb 2015; revised 23 Mar 2015; accepted 23 Mar 2015; published 2 Apr 2015

Table 1. Comparison between simulation and experimental measurements in cornea. The ρ value is obtained by averaging over the whole depth of imaging (30 μm to 100 μm depth), with high enough r-squared for experimental values (see section 4.3).

Objective	**F-SHG**		**B-SHG**	
(Excitation NA)	Simulations	Experiments	Simulations	Experiments
20x (0.95)	1.45	1.45 ± 0.09	1.29	1.22 ± 0.03
40x (1.1)	1.46	1.5 ± 0.07	1.29	1.27 ± 0.04
60x (1.2)	1.46	1.47 ± 0.05	1.28	1.25 ± 0.08

detection. These effects are stronger for higher excitation and detection NAs, but do not change significantly in the range of our experimental studies (0.95-1.2). We attribute the weakness of excitation and detection NAs effects in our experiments to the dispersion and aberrations in real biological tissues, which are remodeling the excitation volume. Spatial excitation patterns in tendon and cornea are then expected to differ from the one in the model system in Fig. 4 without any abberrations and with index matching between the immersion medium and the sample. Numerical simulations show that ρ determination in a strongly focused regime is also affected by other optical parameters such as refractive indexes of immersion medium and sample. Accordingly, the effect of birefringence for ρ determination in tendon can be seen in Fig. 5(a) and 5(b). The measured and simulated anisotropy parameter are oscillating with a ≈ 30 μm period, corresponding to the birefringence reported in [7]. Nevertheless, we have verified numerically and experimentally that the determination of fibril main orientation is not affected by strong focusing, as already reported for cornea [21].

This study has been performed for homogeneous media with in-plane collagen fibrils to understand the role of the setup geometry on ρ measurements in a model configuration. However, the geometry and specific features of the sample itself may affect the measurement of SHG anisotropy. For example, as recently reported [16], an isolated fibril with submicrometer diameter in the excitation volume would have a dramatically different SH radiation pattern, and therefore a different measured SHG anisotropy, than the one for a homogeneous medium. Moreover, this SH radiation pattern would depend on the fibril position in this volume and its diameter. Every specific experimental configuration should therefore be evaluated using numerical simulations and experiments should be performed with different setup geometries to obtain reliable determination of anisotropy parameter ρ.

6. Conclusion

In this study, we demonstrated that measurements of SHG anisotropy parameter are strongly dependent on the geometrical configuration of the setup: they vary slightly with focusing and collecting NA, and significantly with detection direction. Anisotropy is overestimated with forward detection, and underestimated with backward detection. Measurements of orientation are fortunately not impacted by any geometrical parameter and are therefore relevant both in B-SHG and F-SHG [21]. These results are based on a deep understanding of SHG signal build-up and may be generalized to more complex configurations. Most importantly, they are crucial for biomedical applications of P-SHG using *in vivo* imaging. Such experiments indeed require backward detection of SHG signals, while almost all previous P-SHG experiments have been performed with forward detection. The consistency of SHG anisotropy measurements must therefore be carefully examined as a function of detection direction and, to a lesser extent, of focusing NA. Altogether, our study provides a useful tool to build a solid protocol allowing reproducible anisotropy measurements. Provided that the anisotropy parameter has been first measured in a model sample with in-plane geometry, SHG anisotropy should then give reliable

#234705 - $15.00 USD Received 17 Feb 2015; revised 23 Mar 2015; accepted 23 Mar 2015; published 2 Apr 2015

information about out of plane orientation of biopolymers or their disorder in the excitation volume.

Appendix: Theoretical and experimental study of measurement precision

All P-SHG measurements have been done with P polarization angles regularly spaced between 0 and 2π, and N measurements per excitation angle, that is a total of PN measurements. The mean number of photons per measurement is β (see Eq. (4)), and the total mean number of photons is $< N_{tot} >= NP\beta$.

The minimum variance of the two parameters ρ and φ can be theoretically calculated [35] under these experimental conditions. In case of a shot noise (Poisson distribution), those variances are inversely proportional to $< N_{tot} >$:

$$(\Delta\varphi)^2 \geq \frac{1}{2 < N_{tot} > (B^2+4A^2)} \tag{8}$$

$$(\Delta\rho)^2 \geq \frac{1}{< N_{tot} > (1-B+A)^2}[\frac{1}{\rho^2}+\rho^2] \tag{9}$$

Those variances have also been measured on our setup by recording a set of 100 P-SHG images of the same area of a tendon, with the same excitation power, i.e. the same number of detected photons $< N_{image} >$. The set of raw images enables noise measurement at the mean number of detected photons, which is linked to the excitation intensity. In order to get the noise at larger numbers of detected photons, raw images have been summed up. Thus, the summation of a number m of raw images creates artificial images with $m < N_{image} >$ detected photons. The determination of φ and ρ is then repeated in each pixel of the images, for all possible summations of m images. This measurement is done for the raw images and for m from 2 to 50. At the end, mean value and standard deviation for those two parameters are known for different total mean numbers of detected photons $< N_{tot} >= m < N_{image} >$.

Theoretical and experimental results are shown in Fig. 6. They exhibit a good agreement, which shows that the main noise in our setup is indeed the shot noise of detected photons. For the measurements done in this paper, we detect around 200,000-300,000 photons after binning, so $\Delta\varphi < 1^\circ$ and $\Delta\rho < 0.01$.

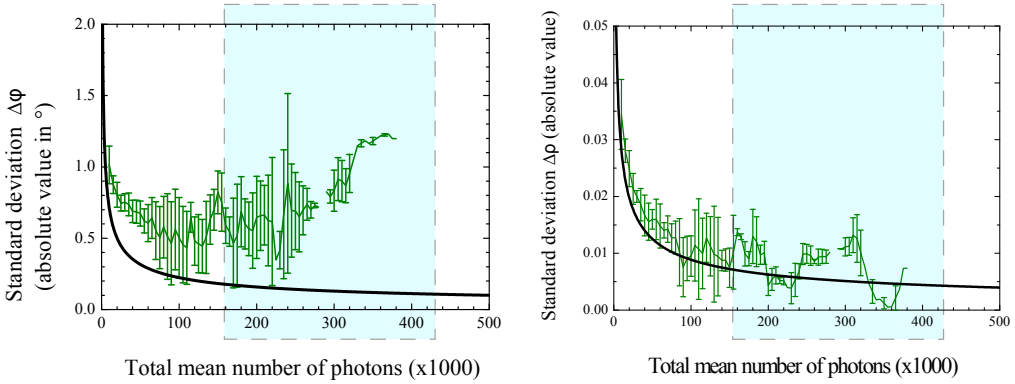

Fig. 6. Precision measurements (— Fit, F-SHG) and theoretical calculation (—) for a Poisson noise. In light blue: usual total mean number of detected photons, considering binning of approx. 400 pixels (for one sub-area) before extracting φ and ρ in order to increase measurements accuracy.

#234705 - $15.00 USD Received 17 Feb 2015; revised 23 Mar 2015; accepted 23 Mar 2015; published 2 Apr 2015

Acknowledgments

The authors gratefully acknowledge I. Sourati and S. Gleyze from the Banque Française des Yeux for providing the human corneas for scientific use, D. Zala from Institut Curie (Orsay) for providing the rat tails, X. Solinas and J.-M. Sintès for technical implementation of the setup. This study was supported by the French National Agency for Research (ANR) under grant ANR-10-INBS-04 (France Bio-Imaging). C. T. was supported by Grant Contrat Doctoral Spécifique Normalien from MESR.

#234705 - $15.00 USD Received 17 Feb 2015; revised 23 Mar 2015; accepted 23 Mar 2015; published 2 Apr 2015